

Controlling Diffusion in Poly-Si Tunneling Junctions for Monolithic Perovskite/Silicon Tandem Solar Cells

Christoph Luderer , Michaela Penn, Christian Reichel, Frank Feldmann , Jan Christoph Goldschmidt , Susanne Richter, Angelika Hähnel , Volker Naumann , Martin Bivour, and Martin Hermle

Abstract—The performance of a low-resistive p^+/n^+ poly-Si tunneling junction (SiTJ) based on a tunnel oxide passivating contact in dependence on the thermal budget of the applied post-deposition treatment is studied. We present two approaches to reduce the performance limiting parasitic dopant interdiffusion and, thus, the contact resistivity, without impairing the passivation quality. Both, carbon-alloying of poly-Si layers and the application of diffusion blocking interlayers are effective means to maintain a low contact resistivity of $\sim 24 \text{ m}\Omega\text{cm}^2$ at high thermal process temperatures of up to 950°C . Those low values are obtained using either a standard furnace anneal or a rapid thermal process (RTP). We report on promising results toward a lean process sequence using only one single fast thermal treatment (RTP-only). As a main result, the flexibility for engineering and fabrication of our SiTJ was markedly improved, eventually facilitating industrially feasible perovskite/silicon tandem solar cells. One aspect being higher post-deposition temperatures needed for, e.g., bottom cell rear side contact formation and the first layers of the perovskite to cell.

Index Terms—Contact resistivity, passivating contact, perovskite-silicon tandem, solar cells, tunneling junction.

I. INTRODUCTION

WITH the recent world record efficiency of 29.5% for a perovskite/silicon tandem [1] exceeding the theoretical efficiency limit of 29.4% for a silicon (Si) single junction [2], tandem solar cells are getting more and more attention from the photovoltaic community. The combination of a perovskite cell on top of a crystalline-Si (c-Si) bottom cell is thereby especially attractive, as they promise high efficiency at affordable costs [3]–[5]. For straightforward module and system integration, the monolithic two-terminal tandem configuration is preferred.

Manuscript received May 5, 2021; revised June 11, 2021; accepted July 21, 2021. Date of publication August 13, 2021; date of current version October 21, 2021. This work was supported by the Fraunhofer Lighthouse Project MaNiTU. (Corresponding author: Christoph Luderer.)

Christoph Luderer, Michaela Penn, Christian Reichel, Jan Christoph Goldschmidt, Martin Bivour, and Martin Hermle are with the Fraunhofer Institute for Solar Energy Systems, 79110 Freiburg, Germany (e-mail: christoph.luderer@ise.fraunhofer.de; michaela.penn@ise.fraunhofer.de; christian.reichel@ise.fraunhofer.de; jan.christoph.goldschmidt@ise.fraunhofer.de; martin.bivour@ise.fraunhofer.de; martin.hermle@ise.fraunhofer.de).

Frank Feldmann is with Solarlab Aiko Europe GmbH, 79110 Freiburg, Germany (e-mail: frank.feldmann@ise.fraunhofer.de).

Susanne Richter, Angelika Hähnel, and Volker Naumann are with the Fraunhofer Center for Silicon Photovoltaics, 06120 Halle (Saale), Germany (e-mail: susanne.richter@esp.fraunhofer.de; angelika.haehnel@esp.fraunhofer.de; volker.naumann@esp.fraunhofer.de).

Color versions of one or more figures in this article are available at <https://doi.org/10.1109/JPHOTOV.2021.3101177>.

Digital Object Identifier 10.1109/JPHOTOV.2021.3101177

Such a configuration requires low-ohmic and transparent interconnection of both subcells. Transparent conductive oxides are widely used to serve that purpose [6]–[8]. An alternative are Si-based tunneling junctions (SiTJs), as first demonstrated in a perovskite/Si tandem cell by Mailoa *et al.* [9], which have the benefit of better refractive index matching between the subcells and thus reducing reflection losses [10]. Additionally, they have the potential to be directly integrated in the processing of the bottom cell's passivating contact [11]–[15]. Compared to silicon heterojunction (SHJ)-based SiTJ, poly-Si-based passivating TJs [11], [14] have the benefit of higher thermal stability, making them compatible with the mainstream Si solar cell structure, i.e., the passivated emitter and rear cell (PERC) technology [16] [see Fig. 1(c)]. Further, a temperature stable bottom cell and SiTJ might be preferable for future application, as lead-free perovskite absorbers are supposed to need annealing temperatures exceeding the stability of SHJ bottom cells [17].

Previously, we presented a low-resistive and passivating SiTJ based on a poly-Si(p^+)/poly-Si(n^+)/ SiO_x /c-Si stack [11]. It was shown that its performance is strongly influenced by dopant interdiffusion during post-deposition thermal treatments. Based on this, in this work, the diffusion behavior for different thermal budgets will be studied. Further, two approaches to reduce parasitic interdiffusion will be presented. Finally, the microstructure of the poly-SiTJ is briefly discussed.

II. EXPERIMENTAL

SiTJ structures were fabricated with two different process routes, as depicted in Fig. 1(a). For both process sequences, $200 \mu\text{m}$ thick planar $1 \Omega\text{cm}$ n-type FZ silicon wafers were used as a substrate. After RCA cleaning, a $\sim 1.2 \text{ nm}$ thin tunnel oxide layer was thermally grown in a furnace at 600°C for 10 min. Subsequently, 20–50 nm thick phosphorus (P)-doped Si layers were deposited on both sides via plasma-enhanced chemical vapor deposition (PECVD), yielding symmetrical a-Si:H(n^+)/ SiO_x /c-Si(n)/ SiO_x /a-Si:H(n^+) structures. For route “FA+RTP,” these structures were exposed to a tube furnace anneal (FA) at 900°C for 10 min to “activate” TOPCon (i.e., poly-crystallization of the phosphorus-doped a-Si:H layer, diffusion of dopants into the absorber and modification of the SiO_x /Si interface). This FA was omitted for samples in route “RTP-only.” Then, 20 nm thick boron (B)-doped PECVD a-Si:H layers were deposited on one side. For some samples, methane gas was introduced in the reactor chamber during PECVD, yielding carbon (C)-alloyed

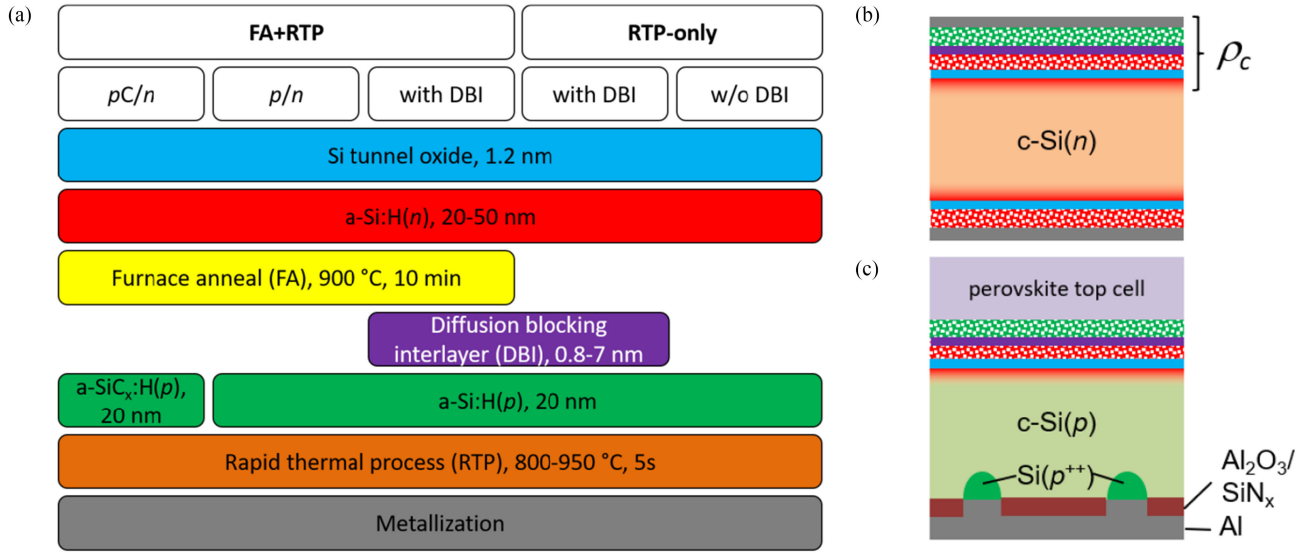


Fig. 1. (a) Process sequences for fabricated SiTJ with (“FA + RTP”) and without FA (“RTP-only”). (b) Sketch of the sample structure for dark J - V measurements. (c) Proposed bottom cell structure with PERC rear side, a front side poly-Si passivating contact and a p⁺/n⁺ poly-SiTJ as subcell interconnection in monolithic perovskite/Si tandem solar cells.

a-SiC_x:H(p⁺). SiTJ comprising such C-alloyed B-doped layers are referred to as pC/n SiTJ. For some other samples, a potential dopant diffusion blocking interlayer (DBI) was deposited directly before a-Si:H(p⁺) deposition. Several DBIs were tested, including SiO_x grown either thermally (“TO”), wet-chemically (“HNO₃”) or via atomic layer deposition (ALD, “SiO_x1” and “SiO_x2”), further PECVD SiC_x and ALD SiN_x. Finally, the samples were exposed to a rapid thermal annealing process (RTP) with peak plateau temperatures T_{RTP} in the range of 800–950 °C and a peak time of 5 s each. To assess the contact resistivity (ρ_c) of the SiTJ, a stack of Ti/Pd/Ag was thermally evaporated on both sides of the samples, which were cut into square 0.5 × 0.5 cm² pieces using a dicing saw. Depicted ρ_c values throughout the text represent the combined junction resistance of both the SiTJ and the tunnel oxide passivated front contact (TOPCon). Bulk and rear contact contributions were subtracted using equally processed symmetric poly-Si(n⁺) reference samples, where the B-doped Si layer was omitted. The implied open-circuit voltage (iV_{oc}) at 1 sun illumination was measured after a hydrogenation step for selected samples as a figure of merit for the passivation quality. Dopant depth profiles were measured with the electrochemical capacitance-voltage (ECV) method and time of flight secondary-ion mass spectroscopy (ToF-SIMS) using an IONTOF TOF.SIMS 5. The Si thin film microstructure was recorded using transmission electron microscopy (TEM) in an image-corrected FEI TITAN3 G2 60-300 with 300 kV electron beam energy.

III. RESULTS

A. Standard p/n SiTJ

Dopant depth profiles of regular p/n SiTJs using the FA+RTP route, as measured with ToF-SIMS, for different post-deposition thermal treatments are shown in Fig. 2. Without any post-deposition thermal treatment (neither FA nor RTP), a high

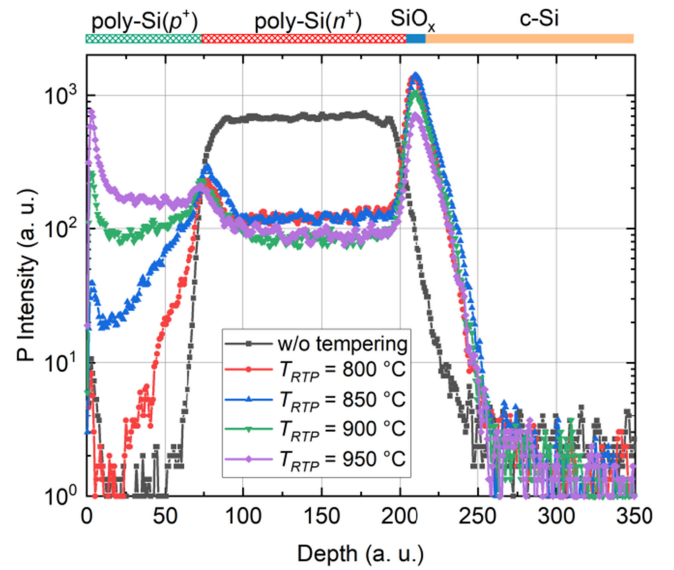


Fig. 2. Dopant depth profiles, as measured with ToF-SIMS, for different post-deposition thermal treatments. The influence of T_{RTP} on the P depth profile is shown.

and homogenous phosphorous (P) concentration was observed within a-Si:H(n⁺) which abruptly decreased to a very low level within a-Si:H(p⁺) and c-Si. The asymmetry in the profile with a slightly lower slope for the tail at the a-Si:H(n⁺)/SiO_x/c-Si interface can be explained by P atoms driven due to the sputtering process during the measurement.

The diffusion of P into the absorber at the poly-Si(n⁺)/SiO_x/c-Si(n) interface, which supports the surface passivation [18], was defined by the FA and hardly changed by the RTP. Within c-Si, the P profiles were very similar independent of T_{RTP} .

The P intensity in the poly-Si(p⁺) layer was increased significantly with increasing T_{RTP} . The P plateau within poly-Si(n⁺)

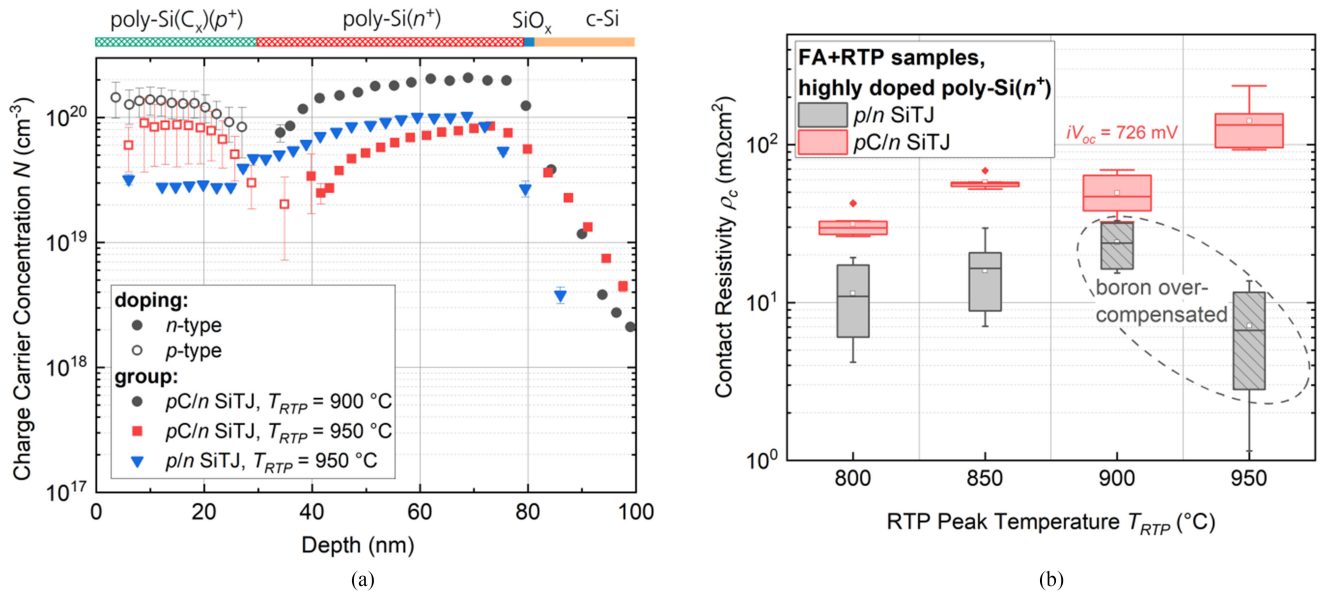


Fig. 3. (a) Active dopant concentration, as measured with ECV, of SiTJ comprising poly-Si(p⁺) with and without incorporated C. (b) ρ_c in dependence of T_{RTP} for p/n and pC/n SiTJ.

was decreased accordingly with increasing T_{RTP} . Apparently, P diffused into the poly-Si(p⁺) region during the RTP with the strength of diffusion determined by the applied thermal budget. Similarly, boron (B) diffusion from the poly-Si(p⁺) into the n⁺-region was enhanced at higher thermal budget (not shown). At $T_{RTP} = 900$ °C, the P concentration was similar in both p-type and n-type poly-Si, and at $T_{RTP} = 950$ °C, the P concentration was even higher in poly-Si(p⁺) compared to poly-Si(n⁺).

Prominent is the peak at the position of the thermally grown SiO_x at the poly-Si/c-Si interface. It is known that SiO_x is a diffusion barrier for P and that P piles up at such oxides [19], [20], which was also previously observed for TOPCon structures [18], [21]. However, quantitative analysis of the peak at the poly-Si/SiO_x interface is difficult due to the so-called SIMS matrix effect, which describes the enhancement of ion yield resulting from the presence of oxygen or cesium [22], [23]. The increase of the P signal toward the poly-Si/air interface probably can be attributed to this effect since the poly-Si surface was oxidized during the RTP. More importantly, a local maximum of the P signal was observed at the position of the SiTJ. This can be explained by a thin native SiO_x present at this interface, despite an HF treatment before a-Si:H(p⁺) deposition. The thin native oxide present at the SiTJ obviously could not provide sufficient dopant diffusion blocking, although a diffusion blocking behavior of the native SiO_x was observed to some extent by comparing SiTJ deposited with and without vacuum break (not shown).

B. Carbon-Alloyed SiTJ

Fig. 3(a) shows the active dopant concentration of a pC/n SiTJ with a carbon (C) content of less than 15 at% in the p⁺-region compared to a regular p/n SiTJ. Both SiTJs comprised a heavily P-doped layer. As previously discussed in [11], at $T_{RTP} = 950$ °C

B was completely overcompensated by P in the p⁺-region of the p/n SiTJ and a fairly high electron concentration of $N > 2.0 \times 10^{19}$ cm⁻³ was measured throughout both poly-Si layers (blue data). Very similar results were obtained for $T_{RTP} = 900$ °C (not shown). Please note that introducing C into the poly-SiC_x(p⁺) leads to uncertainties regarding the absolute N values in the p⁺-region measured with ECV [24]. Nevertheless, it can be stated that C-alloying prevented overcompensation, as p-type doping was measured throughout the whole p⁺-region for both $T_{RTP} = 900$ °C (black data) and 950 °C (red data). From Fig. 3(a), it cannot be concluded how C influenced B or P diffusion specifically. In [25], it was reported that P diffuses in poly-Si predominantly along grain boundaries whereas for B both diffusion along grain boundaries and through crystal grains is important. Since C is known to hamper the self-interstitial diffusion mechanism in Si crystals [26], especially B diffusion might be blocked in C-alloyed poly-Si. Another explanation, why C-alloying prevented overcompensation of B in Fig. 3(a) might be segregation of B to SiC at the SiC/Si interface [27]. Why C-alloying prevented overcompensation of B in Fig. 3(a). However, this cannot explain, that a similar effect was observed when the poly-Si(n⁺) was alloyed with C instead of the poly-Si(p⁺) (not shown).

Comparing ρ_c of the p/n and the pC/n SiTJ in Fig. 3(b), a higher ρ_c was observed for the pC/n SiTJ in the range $T_{RTP} = 800$ –950 °C. The crystalline fraction, obtained by fitting spectroscopic ellipsometry data with a model assuming a mixture of poly-Si, a-Si:H and voids, and therefore also the doping efficiency was decreased considerably in poly-SiC_x with increasing C content (not shown). Consequently, a lower active dopant concentration N at the p⁺/n⁺ poly-Si interface and, thus, a broadened depletion width can be assumed. Hence, at $T_{RTP} = 800/850$ °C, the higher resistance of the pC/n SiTJ can most likely be attributed to less efficient tunneling as a result of

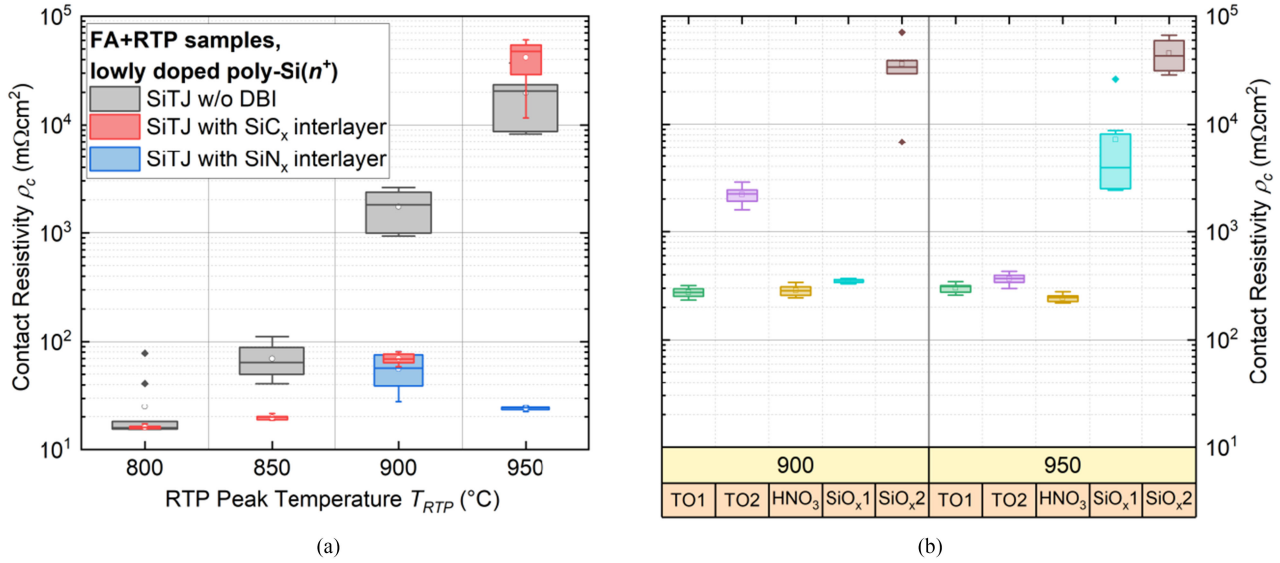


Fig. 4. Resistance in dependence of T_{RTP} for SiTJs comprising different DBIs. (a) ρ_c of FA+RTP SiTJ without DBI as reference and SiTJs with SiN $_x$ or SiC $_x$ DBI. (b) ρ_c of FA+RTP SiTJs with different SiO $_x$ DBIs.

a broadened depletion width [28]–[30]. Further, a higher “bulk” resistivity of the poly-SiC $_x$ layer itself is expected due to a lower crystalline fraction and smaller crystal grains as a result of C-alloying. At $T_{RTP} = 900$ °C and higher temperatures, the p/n structure without C was not a tunneling junction anymore, as B was completely overcompensated by P [11], and the comparison of ρ_c is obsolete. The pC/n SiTJ, however, showed low resistance and good passivation with $\rho_c = 47$ m Ω cm 2 and $iV_{oc} = 726$ mV at $T_{RTP} = 900$ °C. Thus, it is possible to hamper interdiffusion at the poly-SiTJ by C-alloying, thereby increasing the thermal stability of the poly-SiTJ. Another positive effect of C-alloyed poly-SiC $_x$ regarding tandem application is the increased sheet resistance (not shown), which might be beneficial to impair the connection of shunt paths in a tandem device [31]–[33] and to ease up-scaling [12], [34].

C. Diffusion Blocking Interlayer

To show the potential as dopant DBI, ρ_c of several test structures comprising different interlayers at the SiTJ is plotted against T_{RTP} in Fig. 4(a) and (b). The regular p/n SiTJ without interlayer served as a reference (black boxes). Please note that the P dopant concentration was lower compared to the structures shown in Fig. 3, thus, at $T_{RTP} \geq 900$ °C, B was not overcompensated but ρ_c was high for the reference without DBI due to strong interdiffusion. All structures received the FA prior to a-Si:H(p $^+$) deposition and a final RTP step to ensure low-ohmic contact to the c-Si bulk and high sensitivity to differences directly at the SiTJ. Since ρ_c was low (<100 m Ω cm 2) up to $T_{RTP} = 850$ °C even without interlayer, most interlayers were only tested at $T_{RTP} = 900$ °C and $T_{RTP} = 950$ °C.

A 6-nm-thick B-doped SiC $_x$ interlayer (C content of ~ 40 at%) seemed to hamper parasitic interdiffusion very efficiently, as very low ρ_c up to $T_{RTP} = 900$ °C were measured (red boxes). At $T_{RTP} = 800$ °C, the SiC $_x$ did not increase ρ_c compared to

the reference and a clear benefit is visible at 850 and 900 °C. At 950 °C, however, ρ_c degraded significantly and was of the same order of magnitude as the reference. With ultrathin (nominally 0.8 nm) ALD SiN $_x$ also very low ρ_c was obtained (blue boxes). In contrast to the SiC $_x$ interlayer, ρ_c was low even at $T_{RTP} = 950$ °C, outperforming the reference structures by three orders of magnitude (24 m Ω cm 2 vs. $\approx 2.0 \times 10^4$ m Ω cm 2). SiN $_x$ is known for its high density and is, thus, not easily penetrable and effectively blocks diffusion of various elements already at very low thicknesses [35]. Using a slightly thicker SiN $_x$ layer (nominally 1.5 nm) led to high ρ_c around 10^3 m Ω cm 2 independent of T_{RTP} (not shown). Since the diffusion blocking behavior should be as good or even better compared to the thinner SiN $_x$ layer, apparently the tunneling probability through the insulating SiN $_x$ was significantly decreased with increased SiN $_x$ thickness.

For SiO $_x$ interlayers similarly lower thickness was beneficial regarding ρ_c [“SiO $_x$ 1” vs. “SiO $_x$ 2” and “TO1” vs. “TO2,” Fig. 4(b)]. Besides thickness, the stoichiometry of the used oxide is decisive [21], [36]. Thermally grown TO2 was not only slightly thicker than TO1 (1.3 vs. 1.2 nm) but also comprised a higher oxygen content [21]. This makes TO2 less susceptible to the formation of pinholes as compared to TO1 [36], [37]. On one hand, pinholes can facilitate transport across the oxide. On the other hand, pinholes represent local dopant diffusion paths. Thus, the role of pinholes cannot definitively be answered here. While ρ_c for structures including TO1 was similar for both $T_{RTP} = 900$ °C and 950 °C, ρ_c for TO2 was significantly higher compared to TO1 at $T_{RTP} = 900$ °C but decreased to a similar level at $T_{RTP} = 950$ °C.

Despite the more permeable matrix of wet-chemically grown HNO $_3$ oxide [21], similar results to TO1 samples were obtained when including it between n- and p-type poly-Si. A 0.8-nm-thick ALD SiO $_x$ (“SiO $_x$ 1”) interlayer provided similar ρ_c as the previously mentioned oxides in the range of 200–400 m Ω cm 2

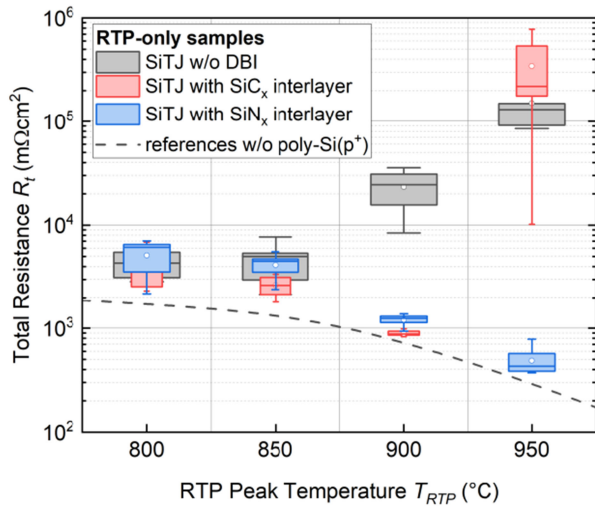


Fig. 5. Total resistance R_t of RTP-only SiTJs, including bulk and rear side contributions. As a guide to the eye, the trend of reference structures where the p-type Si deposition was omitted is represented by the dashed line.

at $T_{RTP} = 900$ °C. However, at 950 °C the oxide seemed to be penetrated by dopants, as higher resistances were measured and no active n-type doping in the poly-Si(n⁺) was detected via ECV (not shown). Hence, in contrast to SiN_x, 0.8 nm of ALD SiO_x were apparently too thin to hold back dopants at this temperature. Moreover, the structure of ALD oxides might be less stoichiometric than that of thermal oxides, since a lower temperature has been used during the ALD process compared to thermal oxidation. This could be another reason why they are less effective diffusion barriers [21]. In [11], we reported that the initial deterioration of the passivation quality due to the RTP can be cured with a standard hydrogenation step. It is worth mentioning, while the passivation quality was not tested for the structures presented in Fig. 4, on similar sister samples the SiN_x and SiC_x interlayers (and presumably also the oxide interlayers) were found not to deteriorate the passivation quality of TOPCon and allowed for $iV_{oc} \approx 725$ mV. It seems reasonable to assume that although the DBI blocks P and B diffusion, smaller hydrogen can still diffuse through it and passivate dangling bonds at the c-Si surface efficiently.

In the lean RTP-only process route (see Fig. 1), high T_{RTP} are necessary for the formation of a low-ohmic contact to the wafer [11]. By counteracting interdiffusion at these high temperatures with a suitable DBI, the realization of a low-resistive SiTJ stack on TOPCon with only one high temperature step might be possible. The most promising interlayers providing the lowest ρ_c , namely PECVD SiC_x and 0.8 nm thick ALD SiN_x, were, thus, also tested in the RTP-only route (Fig. 5). Note that Fig. 5 depicts the total resistance R_t of the structures including bulk and rear side contributions. Whereas the resistance of SiTJs without DBI increased drastically for $T_{RTP} \geq 900$ °C, SiTJs with DBI followed the trend of decreasing R_t of reference structures where the poly-Si(p⁺) was omitted (dashed line in Fig. 5). The SiC_x SiTJ was again degraded at $T_{RTP} = 950$ °C, but the SiN_x SiTJ was still stable at this temperature and provided a reasonable R_t of ≈ 450 mΩcm². This value is mainly limited by the contact to

the wafer and not by the SiTJ. To allow better contact formation to the wafer with RTP-only, the thermally grown Si tunnel oxide was replaced with a wet-chemically grown SiO_x. With this, a SiTJ with very low $\rho_c = 30$ mΩcm² and high $iV_{oc} = 711$ mV was achieved with a single fast high temperature step at $T_{RTP} = 850$ °C (not shown). Unfortunately, in contrast to thermally grown oxides, the thermal stability of the wet-chemical oxide is limited to temperatures below 900 °C. Above 900 °C it cannot provide satisfying surface passivation anymore ($iV_{oc} < 700$ mV) [21], [37]. Thus, the gain in ρ_c due to DBIs, which is highest at $T_{RTP} \geq 900$ °C, cannot be exploited.

D. In-Depth Analysis of SiC_x and SiN_x Interlayers

To visualize diffusion and to distinguish between B and P, ToF-SIMS measurements were conducted on structures exposed to an RTP with $T_{RTP} = 900$ °C. Please note that these samples were not exposed to the FA after a-Si:H(n⁺) and prior to a-Si:H(p⁺) deposition. The profiles were aligned by setting the maximum of the peak at the poly-Si/SiO_x/c-Si interface to a depth of zero. A constant sputter rate was assumed in all layers to convert the sputter time into a sample depth. Without interlayer, P diffused heavily into the nominally p-type region, resulting in a high P concentration throughout both poly-Si layers [see Fig. 6(a)]. The profile evidently resembles the profiles after RTP at $T_{RTP} = 900/950$ °C in Fig. 1(a). In contrast, the profile for the structure comprising the SiN_x interlayer shows the high P diffusion blocking ability of SiN_x. Consequently, the P plateau concentration in poly-Si(n⁺) was higher compared to the sample without interlayer. The SiC_x interlayer also blocked P diffusion, as the P concentration dropped to background noise level in the p-type region. Nevertheless, the P concentration was lower throughout the entire poly-Si(n⁺) region. Presumably P atoms diffused into the 6-nm-thick SiC_x layer but were slowed down and stopped there. Indeed, P enrichment in the SiC_x layer was confirmed by a TEM EDX mapping (not shown).

B diffusion was also efficiently blocked by SiN_x as the B concentration decreased steeply down to noise level within the first few nanometers of the poly-Si(n⁺) [see Fig. 6(b)]. On the contrary, with a SiC_x interlayer, the B concentration decreased not as abruptly and reached deeper into the poly-Si(n⁺), similar to the B profile for the structure without interlayer. One reason why B diffusion is not as efficiently blocked by the SiC_x might be that it is itself heavily B-doped. B diffusion was more pronounced at $T_{RTP} = 950$ °C and resulted in an overcompensation of P in poly-Si(n⁺), as measured with ECV (not shown). Thus, the now completely p-type poly-Si formed a regular p/n junction with the n-type c-Si, explaining the very high ρ_c and diode-like J - V characteristic of structures with SiC_x interlayer at $T_{RTP} = 950$ °C in Figs. 4(a) and 5.

TEM images were recorded to gain insight into the microstructure of the Si layers and the DBI forming the SiTJ. Fig. 7(a) shows a cross-section overview of both poly-Si layers of the SiTJ without DBI on top of the c-Si bulk. The bright contrast at the top left corner corresponds to a C protection layer deposited during lamella preparation. Noticeably, the interface between the p⁺ and n⁺ poly-Si layer is not visible. This could be

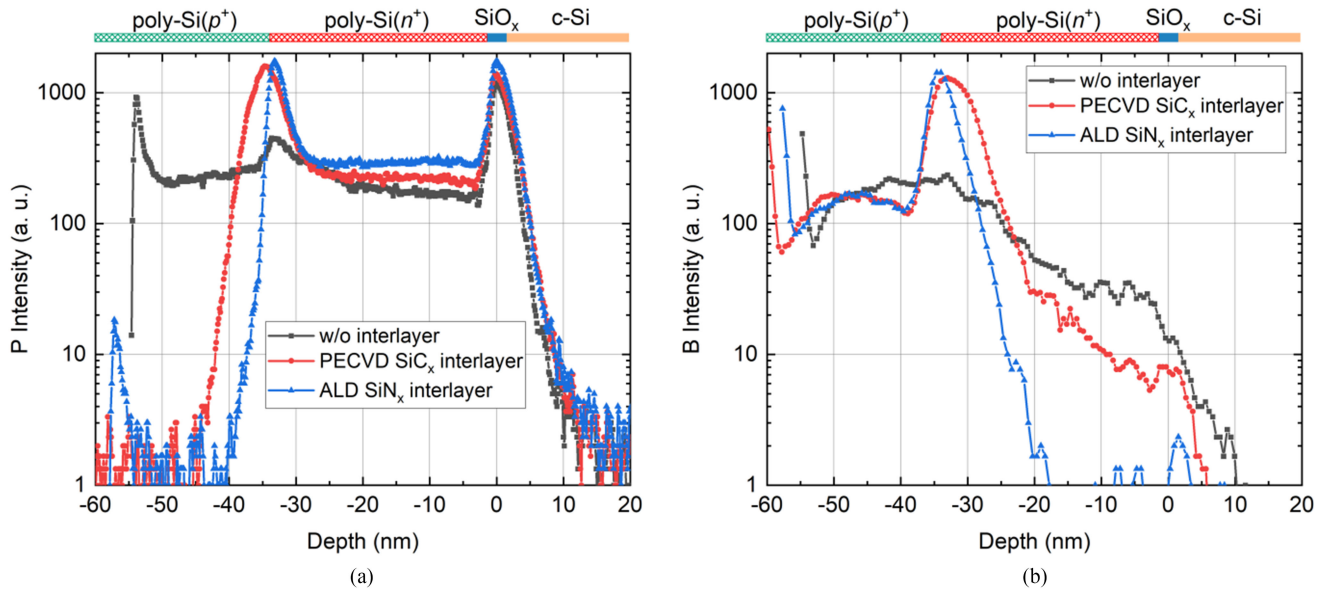


Fig. 6. (a) P and (b) B concentration as measured with ToF-SIMS of SiTJ comprising a PECVD SiC_x interlayer or an ALD SiN_x interlayer in comparison to an SiTJ without interlayer. All samples were exposed to an RTP with T_{RTP} = 900 °C.

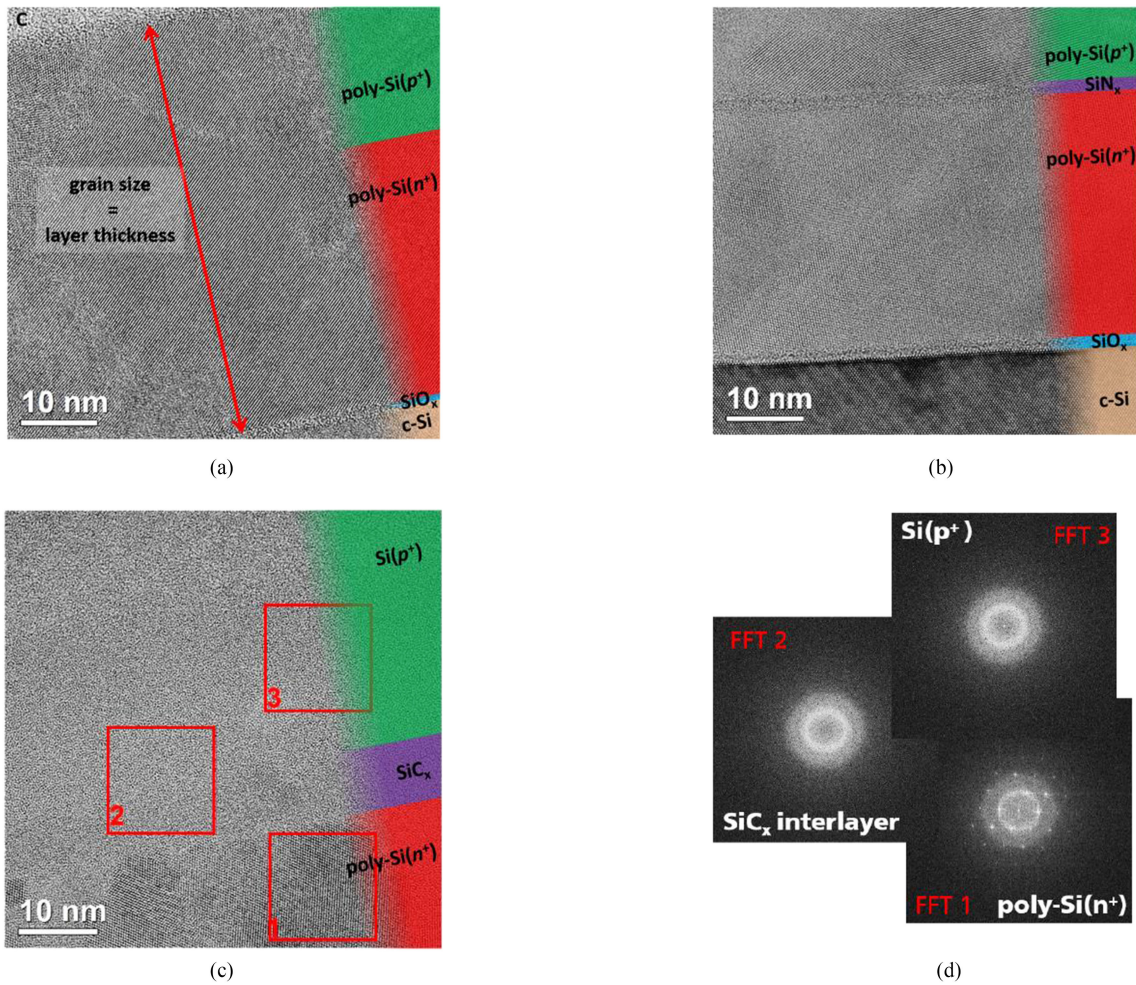


Fig. 7. Microstructure of the SiTJ (a) without DBI, (b) with SiN_x, and (c), (d) with SiC_x interlayer. (d) The FFT of the three red regions of interest in (c), representing the three different thin films. Colored areas in (a), (b), and (c) sketch the sample structure.

explained by a rather rough interface. In that case, the interface position would slightly vary across the thickness of the lamella ($\sim 50\text{--}100$ nm) and clear projection of the interface would not be possible. Consequently, the native oxide at the SiTJ interface, visible in the ToF-SIMS profiles (Figs. 2 and 6), was not detected here. However, an EDX map of this area showed oxygen enrichment at the p^+/n^+ interface (not shown). The amorphous, intentionally thermally grown SiO_x at the poly-Si/c-Si interface was clearly distinguished from the adjacent (poly-)crystalline Si [see Fig. 7(a)]. In some cases, crystal grains spread across the entire combined poly-Si layer thickness of roughly 50 nm. This shows that the SiTJ interface was not very distinct and the native oxide was not thick enough to separate both poly-Si layers. In general, dopant diffusion in poly-Si is much faster along grain boundaries compared to the migration through Si crystal grains [38], [39], thus large grains rather hamper diffusion. Nevertheless, grain boundaries spreading across the p^+/n^+ Si interface might act as fast diffusion paths and facilitate parasitic interdiffusion.

On the cross-section overview of the SiTJ with SiN_x interlayer [see Fig. 7(b)], it is noticeable that the nitride layer is clearly visible, separating the different doped Si layers. Both the doped layers were clearly poly-crystalline, as without DBI. Again, in some cases, grains spread across the entire thickness of the respective poly-Si layer but were separated by the thin amorphous SiN_x interlayer.

Fig. 7(c) shows a cross-section of the SiTJ with SiC_x interlayer. On closer examination of the multilayer stack, significant differences appeared between the different layers. Whereas the P-doped layer was again clearly poly-crystalline, in the SiC_x and the B-doped Si layer no larger scale grains were visible [see Fig. 7(c)]. In the three red marked regions of interest, representing poly-Si(n^+) (FFT1), the SiC_x interlayer (FFT2), and Si(p^+) (FFT3), the signal was undertaken a fast Fourier transformation (FFT) to display the crystal lattice in reciprocal space [see Fig. 7(d)]. Note that FFT2 covers both SiC_x and Si(p^+). FFT1 showed circular brightness contrasts, corresponding to the amorphous phase with no long-range order, overlaid with a clear dot pattern, representing the lattice of the grain. FFT2 and FFT3 showed no sign of long-range order; only the amorphous phase was visible. For the SiC_x layer, this can be readily understood, since due to the high C content of roughly 40 at% crystallization was impeded and higher temperatures above 900°C are necessary to crystallize SiC_x with such a high C content [40]. The Si(p^+) layer was deposited subsequently without vacuum break, which lead to some C contamination (C content $\sim 5\text{at}\%$) according to an EDX line scan (not shown). Nevertheless, very high active dopant concentrations N close to $1.0 \times 10^{20} \text{ cm}^{-3}$ were measured with ECV in the Si(p^+) layer (not shown), which would not be possible in a completely amorphous layer [41], [42]. Since a TEM lamella represents only a small fraction of the whole sample, it might be possible that an amorphous section was selected coincidentally. This scenario is, however, very unlikely. Another important aspect is the orientation of the lamella to the incident electron beam. A crystal grain is only visible if the Bragg's law is fulfilled. Yet, although the lamella was tilted in several orientations, the image

was basically unchanged, and no crystal grains appeared. It is also possible that very small grains on the nanometer scale are present with a broad distribution of orientation, which would make them appear as amorphous phase or not detectable in the FFT. This could explain the high activation of dopants measured in ECV. Lastly, damage of the Si(p^+) layer during lamella preparation that caused its amorphization cannot be ruled out completely. Evidence for that is the further increased C content in the Si(p^+) layer close to the C protection layer detected via EDX and the rougher Si(p^+) surface compared to the lamella without DBI (not shown).

IV. CONCLUSION

A p^+/n^+ poly-SiTJ based on TOPCon was presented. Depending on the applied thermal budget, significant interdiffusion of dopants was observed, limiting the SiTJ performance by drastically increasing ρ_c or by yielding an isotype structure due to complete overcompensation of one dopant species. Two approaches have been presented that prevent such parasitic interdiffusion and thereby improving the thermal stability of the SiTJ: C-alloying of the poly-Si layers and/or utilizing a DBI at the SiTJ. The ability to block P and B diffusion was studied for the most promising interlayers, ALD SiN_x and PECVD SiC_x . Further, the microstructure of the SiTJ was studied via TEM. It was also possible to show that a lean process sequence using only one single fast thermal treatment can enable a low-resistive and well-passivating SiTJ.

The improved thermal stability of the SiTJ eases its device integration such as into an industrially feasible Si bottom solar cell for tandem application based on PERC with the P-doped emitter replaced by a TOPCon front contact.

ACKNOWLEDGMENT

The authors would like to thank A. Leimenstoll, F. Schätzle, and J. Polzin for sample preparation.

REFERENCES

- [1] NREL Best Research-Cell Efficiency Chart. 2021. [Online]. Available: <https://www.nrel.gov/pv/cell-efficiency.html>
- [2] A. Richter, M. Hermle, and S. W. Glunz, "Reassessment of the limiting efficiency for crystalline silicon solar cells," *IEEE J. Photovolt.*, vol. 3, no. 4, pp. 1184–1191, Oct. 2013.
- [3] M. A. Green, "Silicon wafer-based tandem cells: The ultimate photovoltaic solution?," in *Proc. 28th Eur. Photovolt. Sol. Energy Conf. Exhib.*, Paris, France, 2013, pp. 7–10.
- [4] C. Messmer *et al.*, "The race for the best silicon bottom cell: Efficiency and cost evaluation of perovskite-silicon tandem solar cells," *Prog. Photovolt.: Res. Appl.*, vol. 29, pp. 744–759, 2020.
- [5] S. E. Sofia *et al.*, "Roadmap for cost-effective, commercially-viable perovskite silicon tandems for the current and future PV market," *Sustain. Energ. Fuels*, vol. 4, no. 2, pp. 852–862, 2020.
- [6] R. L. Z. Hoye *et al.*, "Developing a robust recombination contact to realize monolithic perovskite tandems with industrially common p-type silicon solar cells," *IEEE J. Photovolt.*, vol. 8, no. 4, pp. 1023–1028, Jul. 2018.
- [7] K. A. Bush *et al.*, "23.6%-efficient monolithic perovskite/silicon tandem solar cells with improved stability," *Nat. Energy*, vol. 2, no. 4, 2017, Art. no. 17009.
- [8] S. Albrecht *et al.*, "Monolithic perovskite/silicon-heterojunction tandem solar cells processed at low temperature," *Energy Environ. Sci.*, vol. 9, no. 1, pp. 81–88, 2016.

- [9] J. P. Mailoa *et al.*, "A 2-terminal perovskite/silicon multijunction solar cell enabled by a silicon tunnel junction," *Appl. Phys. Lett.*, vol. 106, no. 12, 2015, Art. no. 121105.
- [10] D. T. Grant, K. R. Catchpole, K. J. Weber, and T. P. White, "Design guidelines for perovskite/silicon 2-terminal tandem solar cells: An optical study," *Opt. Exp.*, vol. 24, no. 22, pp. A1454–A1470, 2016.
- [11] C. Luderer, C. Reichel, F. Feldmann, M. Bivour, and M. Hermle, "Passivating and low-resistive poly-Si tunneling junction enabling high-efficiency monolithic perovskite/silicon tandem solar cells," *Appl. Phys. Lett.*, vol. 115, no. 18, 2019, Art. no. 182105.
- [12] F. Sahli *et al.*, "Improved optics in monolithic perovskite/silicon tandem solar cells with a nanocrystalline silicon recombination junction," *Adv. Energy Mater.*, vol. 8, no. 6, 2017, Art. no. 1701609.
- [13] F. Sahli *et al.*, "Fully textured monolithic perovskite/silicon tandem solar cells with 25.2% power conversion efficiency," *Nature Mater.*, vol. 17, no. 9, pp. 820–826, 2018. [Online]. Available: <https://www.nature.com/articles/s41563-018-0115-4.pdf>
- [14] R. Peibst *et al.*, "From PERC to tandem //from PERC to tandem: POLO- and p^+/n^+ poly-Si tunneling junction as interface between bottom and top cell: POLO- and p^+/n^+ poly-Si tunneling junction as interface between bottom and top cell," *IEEE J. Photovolt.*, vol. 9, no. 1, pp. 49–54, Jan. 2019. [Online]. Available: <https://ieeexplore.ieee.org/ielx7/5503869/5986669/08533392.pdf?tp=&arnumber=8533392&isnumber=5986669>
- [15] A. Puaud, A.-S. Ozanne, L.-L. Senaud, D. Munoz, and C. Roux, "Microcrystalline silicon tunnel junction for monolithic tandem solar cells using silicon heterojunction technology," *IEEE J. Photovolt.*, vol. 11, no. 1, pp. 58–64, Jan. 2021.
- [16] International Technology Roadmap for Photovoltaic, 2019. Accessed: Oct. 9, 2020. [Online]. Available: www.itrpv.net
- [17] X. Yang, W. Wang, R. Ran, W. Zhou, and Z. Shao, "Recent advances in $\text{Cs}_2\text{AgBiBr}_6$ -based halide double perovskites as lead-free and inorganic light absorbers for perovskite solar cells," *Energy Fuels*, vol. 34, no. 9, pp. 10513–10528, 2020.
- [18] F. Feldmann, J. Schön, J. Niess, W. Lerch, and M. Hermle, "Studying dopant diffusion from poly-Si passivating contacts," *Sol. Energy Mater. Sol. Cells*, vol. 200, 2019, Art. no. 109978.
- [19] J. S. Johannessen, W. E. Spicer, J. F. Gibbons, J. D. Plummer, and N. J. Taylor, "Observation of phosphorus pile-up at the SiO_2 -Si interface," *J. Appl. Phys.*, vol. 49, no. 8, pp. 4453–4458, 1978.
- [20] S. A. Schwarz, R. W. Barton, C. P. Ho, and C. R. Helms, "Studies of phosphorus pile-up at the Si-SiO₂ interface using Auger sputter profiling," *J. Electrochem. Soc.*, vol. 128, no. 5, pp. 1101–1106, 1981.
- [21] J.-I. Polzin *et al.*, "Temperature-induced stoichiometric changes in thermally grown interfacial oxide in tunnel-oxide passivating contacts," *Sol. Energy Mater. Sol. Cells*, vol. 218, 2020, Art. no. 110713.
- [22] V. R. Deline, W. Katz, C. A. Evans, and P. Williams, "Mechanism of the SIMS matrix effect," *Appl. Phys. Lett.*, vol. 33, no. 9, pp. 832–835, 1978.
- [23] V. E. Krohn, "Emission of negative ions from metal surfaces bombarded by positive cesium ions," *J. Appl. Phys.*, vol. 33, no. 12, pp. 3523–3525, 1962.
- [24] B. Steinhauser, "Passivating dopant sources for high-efficiency n-type silicon solar cells," Dissertation, Universität Konstanz, Baden-Württemberg, Germany, 2017.
- [25] B. Han *et al.*, "Phosphorus and boron diffusion paths in polycrystalline silicon gate of a trench-type three-dimensional metal-oxide-semiconductor field effect transistor investigated by atom probe tomography," *Appl. Phys. Lett.*, vol. 107, no. 2, 2015, Art. no. 23506.
- [26] H. Rücker *et al.*, "Suppressed diffusion of boron and carbon in carbon-rich silicon," *Appl. Phys. Lett.*, vol. 73, no. 12, pp. 1682–1684, 1998.
- [27] M. Schnabel *et al.*, "Boron diffusion in nanocrystalline 3C-SiC," *Appl. Phys. Lett.*, vol. 104, no. 21, 2014, Art. no. 213108.
- [28] C. Messmer, M. Bivour, J. Schon, S. W. Glunz, and M. Hermle, "Numerical simulation of silicon heterojunction solar cells featuring metal oxides as carrier-selective contacts," *IEEE J. Photovolt.*, vol. 8, no. 2, pp. 456–464, 2018.
- [29] S. Kirner *et al.*, "The influence of ITO dopant density on J-V characteristics of silicon heterojunction solar cells: Experiments and simulations," *Energy Procedia*, vol. 77, pp. 725–732, 2015. [Online]. Available: <https://depositonce.tu-berlin.de/bitstream/11303/7616/1/1-s2.0-S1876610215008711-main.pdf>
- [30] P. Procel *et al.*, "The role of heterointerfaces and subgap energy states on transport mechanisms in silicon heterojunction solar cells," *Prog. Photovolt. Res. Appl.*, vol. 28, no. 9, pp. 935–945, 2020.
- [31] M. Despeisse *et al.*, "Resistive interlayer for improved performance of thin film silicon solar cells on highly textured substrate," *Appl. Phys. Lett.*, vol. 96, no. 7, 2010, Art. no. 73507.
- [32] P. Buehlmann *et al.*, "In situ silicon oxide based intermediate reflector for thin-film silicon micromorph solar cells," *Appl. Phys. Lett.*, vol. 91, no. 14, 2007, Art. no. 143505.
- [33] C. Blaga *et al.*, "Palliating the efficiency loss due to shunting in perovskite/silicon tandem solar cells through modifying the resistive properties of the recombination junction," *Sustain. Energy Fuels*, vol. 5, pp. 2036–2045, 2021.
- [34] J. Zheng *et al.*, "Large area efficient interface layer free monolithic perovskite/homo-junction-silicon tandem solar cell with over 20% efficiency," *Energy Environ. Sci.*, vol. 11, no. 9, pp. 2432–2443, 2018.
- [35] V. Y. Doo, "Silicon nitride, a new diffusion mask," *IEEE Trans. Electron Devices*, vol. ED-13, no. 7, pp. 561–563, Jul. 1966.
- [36] J.-I. Polzin, F. Feldmann, B. Steinhauser, M. Hermle, and S. W. Glunz, "Study on the interfacial oxide in passivating contacts," in *Proc. SiliconPV 9th Int. Conf. Crystalline Silicon Photovolt.*, 2019, Art. no. 40016.
- [37] A. Moldovan *et al.*, "Tunnel oxide passivated carrier-selective contacts based on ultra-thin SiO_2 layers grown by photo-oxidation or wet-chemical oxidation in ozonized water," in *Proc. IEEE 42nd Photovolt. Specialist Conf.*, New Orleans, LA, USA, 2015, pp. 1–6.
- [38] I. Post and P. Ashburn, "Investigation of boron diffusion in polysilicon and its application to the design of p-n-p polysilicon emitter bipolar transistors with shallow emitter junctions," *IEEE Trans. Electron Devices*, vol. 38, no. 11, pp. 2442–2451, Nov. 1991.
- [39] H. J. Queisser, K. Hubner, and W. Shockley, "Diffusion along small-angle grain boundaries in silicon," *Phys. Rev.*, vol. 123, no. 4, pp. 1245–1254, 1961.
- [40] L. Calcagno, P. Musumeci, F. Roccaforte, C. Bongiorno, and G. Foti, "Crystallization process of amorphous silicon-carbon alloys," *Thin Solid Films*, vol. 411, no. 2, pp. 298–302, 2002.
- [41] W. E. Spear and P. G. Le Comber, "Substitutional doping of amorphous silicon," *Solid State Commun.*, vol. 17, no. 9, pp. 1193–1196, 1975.
- [42] C. Luderer, L. Tutsch, C. Messmer, M. Hermle, and M. Bivour, "Influence of TCO and a-Si:H doping on SHJ contact resistivity," *IEEE J. Photovolt.*, vol. 11, no. 2, pp. 329–336, Mar. 2021.